applied sciences

MDPI

Article

Defect-Induced Modulation of a 2D ZnO/Graphene Heterostructure: Exploring Structural and Electronic Transformations

Ivan Shtepliuk [1,2]

[1] Semiconductor Materials Division, Department of Physics, Chemistry and Biology-IFM, Linköping University, S-58183 Linköping, Sweden; ivan.shtepliuk@liu.se
[2] I.M. Frantsevich Institute for Problems of Materials Science, N.A.S. of Ukraine, 3, Krzhizhanovsky Str., 03142 Kyiv, Ukraine

Abstract: This paper presents a theoretical study on the effects of selected defects (oxygen vacancies and substitutional Fe_{Zn} atoms) on the structural and electronic properties of a 2D ZnO/graphene heterostructure. Spin-polarized Hubbard- and dispersion-corrected density functional theory (DFT) was used to optimize the geometrical configurations of the heterostructure and to analyze the equilibrium distance, interlayer distance, adhesion energy, and bond lengths. Charge density difference (CDD) analysis and band structure calculations were also performed to study the electronic properties of the heterostructure. The results show that the presence of defects affects the interlayer distance and adhesion energy, with structures including oxygen vacancies and Fe_{Zn} substitutional atoms having the strongest interaction with graphene. It is demonstrated that the oxygen vacancies generate localized defect states in the ZnO bandgap and lead to a shift of both valence and conduction band positions, affecting the Schottky barrier. In contrast, Fe dopants induce strong spin polarization and high spin density localized on Fe atoms and their adjacent oxygen neighbors as well as the spin asymmetry of Schottky barriers in 2D ZnO/graphene. This study presents a comprehensive investigation into the effects of graphene on the electronic and adsorption properties of 2D ZnO/graphene heterostructures. The changes in electronic properties induced by oxygen vacancies and Fe dopants can enhance the sensitivity and catalytic activity of the 2D ZnO/graphene system, making it a promising material for sensing and catalytic applications.

Keywords: 2D ZnO; van der Waals heterostructure; graphene; spin-polarized density functional theory; band structure; defect engineering; hydrogen adsorption

check for updates

Citation: Shtepliuk, I. Defect-Induced Modulation of a 2D ZnO/Graphene Heterostructure: Exploring Structural and Electronic Transformations. *Appl. Sci.* **2023**, *13*, 7243. https://doi.org/10.3390/app13127243

Academic Editor: Yoong Ahm Kim

Received: 2 May 2023
Revised: 6 June 2023
Accepted: 16 June 2023
Published: 17 June 2023

Copyright: © 2023 by the author. Licensee MDPI, Basel, Switzerland. This article is an open access article distributed under the terms and conditions of the Creative Commons Attribution (CC BY) license (https://creativecommons.org/licenses/by/4.0/).

1. Introduction

Two-dimensional zinc oxide (2D ZnO) is a novel promising material for catalytic, sensing, energy storage, and optoelectronics applications [1–10]. The great potential of this graphene-like wide-band-gap material mainly originates from its unique properties, which can even outperform those of bulk ZnO [11]. For example, the fact that the 2D ZnO has an atomically thick, flat surface implies that all surficial atoms are available for the interaction with foreign atoms or molecules, making this material catalytically active and extremely sensitive to external stimuli. Therefore, during the last ten years, intensive research efforts have been devoted to the synthesis and theoretical investigation of the ZnO monolayer [12–15].

A combination of 2D ZnO with graphene in a synergistic manner is a promising and effective strategy to extend the initial functionality of 2D ZnO through designing van der Waals (vdW) 2DZnO/graphene heterostructures with improved optical and charge transfer properties [16–18]. Marfoua and Hong [18] demonstrated the remarkable advantages associated with integrating ZnO and graphene in a heterostructure. One notable benefit is the

significantly prolonged carrier relaxation time compared to ZnO in isolation, resulting in enhanced carrier mobility, electrical conductivity, and electronic thermal conductivity within the heterostructure. Moreover, the heterostructure exhibits approximately five-times-higher lattice thermal conductivity than ZnO alone. Additionally, Sahatiya et al. [17] reported a remarkable 87% improvement in UV-light photosensing in a 2D ZnO/graphene heterostructure under a compressive strain. In this regard, it is crucially important to comprehend the fundamental properties of 2DZnO/graphene heterostructures, especially considering a realistic structure of 2D ZnO that may include point defects, such as oxygen vacancies or substitutional defects. Given that defect engineering is an important strategy for tailoring the properties of two-dimensional materials [19,20], achieving an in-depth understanding of the effects of different types of defects in 2D ZnO on the electronic, contact, and catalytic properties of the 2DZnO/graphene heterostructure is highly demanded. Despite the previous research that provided insights into the mechanisms underlying the formation of point defects and their effect on the selected properties of 2D ZnO supported by graphene [21–25], some issues related to spin-dependent electronic and contact properties, as well the catalytic properties of defective 2DZnO/graphene heterostructures, still need to be resolved. More specifically, spin selectivity effects on defect-engineered 2DZnO/graphene systems and the hydrogen evolution reaction (HER) in these heterogeneous vdW heterostructures have been poorly investigated. To demonstrate the potential of defect engineering for optimizing 2DZnO/graphene heterostructure properties for specific applications, two representative types of points defects are investigated in this work: neutral oxygen vacancies and Fe substitutional atoms.

This paper aims to provide a comprehensive theoretical framework for understanding the impact of defects in 2D ZnO supported by graphene on its physical properties, and to guide the design of future experiments for optimizing its functionalities for specific applications. The influence of a wide range of defects, including Fe substitutional defects and oxygen vacancies, on the electronic band structure and contact and charge transfer properties of the 2D ZnO/graphene heterostructure are explored by employing state-of-the-art spin-polarized GGA-PBE+U-D2 calculations. The catalytic activity of defect-engineered 2D ZnO/graphene heterostructures towards the hydrogen evolution reaction is in special focus. The results of this study not only have implications for catalytic applications, but also for other areas, such as optoelectronics, sensing, and energy storage, where the properties of 2D ZnO supported by graphene are of significant interest and importance.

2. Methods

Spin-polarized density functional theory (DFT) calculations using the SIESTA code [26] were performed to investigate the effects of different types of defects on the structure, electronic, and catalytic properties of 2D ZnO supported by graphene. A generalized gradient approximation (GGA) of Perdew–Burke–Ernzerhof (PBE) functional [27] combined with a double-ζ polarized (DZP) basis set was employed. Since a 2D ZnO/graphene system can be referred to as a van der Waals (vdW) heterostructure [3], Grimme's D2 empirical correction [28] was included in the calculations to consider the vdW interaction between 2D ZnO and graphene layers. To generate Grimme potential parameters, *fdf2grimme* utility was used. The GGA-PBE functional is known to underestimate the ZnO band gap [29], and the Hubbard *U* correction (DFT + U_d + U_p) [30] was therefore applied to provide a more correct representation of the electronic structure of 2D ZnO. These parameters, U_d = 10 eV and U_p = 7 eV, were selected because they effectively reconciled theoretical predictions with the experimental data [31]. For relaxation-type calculations, a *k*-grid of 9 × 9 × 1 Monkhorst–Pack was used to sample the Brillouin zone. For band-structure calculations, partial density of states (PDOSs), spin density, and charge transfer properties, finer sampling with a *k*-grid size of 24 × 24 × 1 *k*-points was utilized. For all calculations, the energy shift was set to 200 meV and the force tolerance was set to 0.02 eV $Å^{-1}$. A convergence tolerance of 0.02 eV/Å was selected as it provided a balance between the computational cost and accuracy in capturing the relevant physical properties of interest [32–35]. However, to

ensure the robustness of the findings, additional calculations were performed with a tighter force convergence tolerance of 0.01 eV/Å. The results demonstrate that the adhesion energy (Table S1, Supplementary Material) and band structure of all considered systems remain unchanged (Figures S1–S5, Supplementary Material), suggesting that the initial choice of 0.02 eV/Å was sufficient to capture the essential physics and achieve accurate results within the scope of the study. Norm-conserving Troullier–Martins pseudopotentials for Zn, O, C, Fe, and H atoms were generated using the ATOM code [36].

The two-dimensional ZnO/graphene heterostructure was constructed by stacking a 3 × 3 ZnO monolayer on top of a 4 × 4 graphene. The initial choice of unit cell sizes was based on previous studies [13]. According to the available literature data, the lattice mismatch between the 4 × 4 graphene and 3 × 3 ZnO was about 0.59%. In this study, a full optimization procedure was performed to determine the appropriate unit cell sizes and achieve an accurate representation of the stacking structure.

To simulate the formation of oxygen vacancies and Fe-to-Zn substitutional defects, the starting point was a perfect structure of 2D ZnO with one or two oxygen atoms removed from the lattice, as well as with one or two Zn atoms replaced by Fe atoms. In this study, all atomic coordinates, including those of graphene, were allowed to relax during the calculations. This meant that the local structure and composition of ZnO, such as oxygen vacancies and substitutional Fe defects, could potentially influence the local structure of the graphene.

In the final stage of the study, the catalytic activity of pristine and defect-engineered 2D ZnO supported by graphene for the hydrogen evolution reaction (HER) was assessed using the slab model and the (DFT+U)-D2 method. HER was modeled by analyzing the Volmer reaction and predicting the Gibbs free energy of hydrogen adsorption (ΔG_{H^*}) [37].

Overall, the proposed methodology provided a comprehensive investigation of the defect effect on the properties of 2D ZnO/graphene heterostructures, from their structure to their electronic, contact, and catalytic properties.

3. Results and Discussion

3.1. Structural Properties

Figure 1 shows the optimized geometrical configurations of the 2D ZnO/graphene heterostructure predicted by DFT, highlighting the effect of defects (oxygen vacancies and substitutional Fe_{Zn} atoms) on the 2D ZnO morphology and interlayer distance. The equilibrium distance between the pristine ZnO monolayer and graphene was estimated to be 2.931 Å, which was smaller than the same parameter reported by other authors (DFT-D2+U: 3.134 Å [38], GGA(PBE)-D2: 3.556 Å [13]). The fact that the structural parameters and electronic properties of 2D materials are usually method- and functional-dependent mainly explains this difference. However, a unique stacking configuration of a bilayer heterostructure modeled within this work could not be ruled out as a possible factor influencing the interlayer interaction. It was also observed that, independently on the defect type, 2D ZnO layers lay flat on the graphene surface. Table S2 (Supplementary Material) summarizes the *z*-coordinates of graphene carbon atoms in the considered systems. The observed similarity in the coordinates of carbon atoms in all models suggests that the local structure of graphene was hardly affected by the surrounding environment, including the presence of defects and doping in ZnO. When separately considering vacancy-containing and Fe-doped systems, it was evident that the stronger interaction between defective 2D ZnO and graphene, compared to that between pristine 2D ZnO and graphene, was manifested by a shorter interlayer distance. The structures, including 2 oxygen vacancies and 2 Fe_{Zn} substitutional atoms, were characterized by the smallest values of the interlayer distance: 2.913 Å and 2.912 Å, respectively. This was consistent with the calculations of the adhesion energy. More specifically, the adhesion energy of pristine 2D ZnO on the graphene surface was predicted to be −0.076 eV per atom. While for the systems with 2 oxygen vacancies and 2 Fe_{Zn} substitutional atoms, E_{adh} achieved more negative values (Table 1), pointing out a stronger interaction between the 2D ZnO layer and graphene.

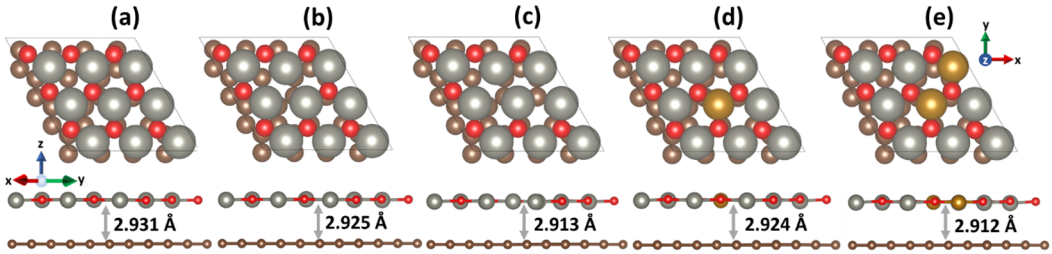


Figure 1. Optimized structures of (**a**) pristine and (**b**–**d**) defect-engineered 2D ZnO/graphene heterostructures, including: (**b**) 1 oxygen vacancy, (**c**) 2 oxygen vacancies, (**d**) 1 Fe substitutional atoms, and (**e**) 2 Fe substitutional atoms, respectively. Grey-, red-, mustard-, and brown-colored balls represent zinc, oxygen, iron, and cardon atoms, respectively.

Table 1. Summary of selected parameters for pristine and defective 2D ZnO/graphene structures obtained by spin-polarized GGA-PBE+U-D2 calculations. The main parameters describing the electronic properties of the heterostructure are given for the spin-up channel. The parameters for spin-down channels are included in square brackets.

Structure	D, Å	Mean Zn-O Bond Length, Å	E_{adh}, eV	E_D, eV	Φ_n, eV	Φ_p, eV
2D ZnO/G	2.931	2.001	−0.076	0 [0]	1.578 [1.571]	0.520 [0.516]
$1V_O$-2D ZnO/G	2.925	2.022	−0.077	−0.231 [−0.231]	1.354 [1.354]	0.636 [0.635]
$2V_O$-2D ZnO/G	2.913	2.027	−0.080	−0.524 [−0.524]	0.915 [0.915]	−0.016 [−0.018]
1Fe-2D ZnO/G	2.924	2.019	−0.091	−0.619 [−0.643]	0.931 [0.897]	1.508 [0]
2Fe-2D ZnO/G	2.912	2.032	−0.096	−0.663 [−0.691]	0.816 [0.832]	1.495 [0]

It is interesting to note that the energy cost associated with the removal of oxygen atoms and the Fe-to-Zn substitution mechanism was compensated by the elongation of the Zn–O bonds (Table 1). In the case of heterostructures comprising the oxygen vacancies, zinc atoms that surrounded the vacant site(s) tended to approach each other, thereby causing a redistribution of chemical bonds in the overall structure. On the other hand, in the Fe-containing complexes, the local formation of the Fe-O bonds, which are generally stronger and shorter than Zn–O bonds (~1.9 Å vs. ~2.0 Å), was the main reason for the increase in the mean Zn–O bond length. The observed difference in the bond length can be understood in terms of atomic radii and electronic configuration. Indeed, since the iron atom has a smaller atomic radius compared to the Zn atom, it can exert a stronger attractive force on the oxygen atom's electrons compared to the zinc. Furthermore, compared to the completely filled *d*-orbital of the Zn atom, the partially filled *d*-orbital of Fe made it more effective in bonding with the oxygen (a more efficient overlap with the oxygen *p*-orbitals was expected). The combination of these factors explains the shorter and stronger Fe–O bond compared to the Zn–O bond.

3.2. Electronic Properties

To comprehend the electronic properties of the 2D ZnO/graphene heterostructures, CDD analysis and band structure calculations were performed. As shown in Figure 2a, the charge accumulation (yellow-colored region) occurs mainly in the middle of the pristine 2D ZnO/graphene structure. This is also evidenced by an appearance of a strong CDD peak in the corresponding region of the *xy*-plane averaged charge redistribution curve presented

in Figure 2b. In turn, the other two charge accumulation regions (as well as the maxima of the CDD curve) are located directly in 2D ZnO and graphene layers, while the charge depletion regions are manifested as deep minima of CDD curves were observed below (above) the 2D ZnO (graphene) layer. The nature of the charge redistribution in the system leads to the coincidence of the Dirac point energy with the Fermi level (Figure 2c). This was probably because the positive and negative charge carriers canceled each other out, making the graphene charge neutral. It is noteworthy that the band structure and density of states of the pristine 2D ZnO/graphene system were the same for the spin-up and spin-down channels. The conduction band mainly consisted of C 2*p* states, while the contribution from unoccupied Zn 4*s* states became evident above 2 eV. The valence band was mainly dominated by the occupied O 2*p* states; however, the contribution of occupied C 2*p* and Zn-related states was also significant.

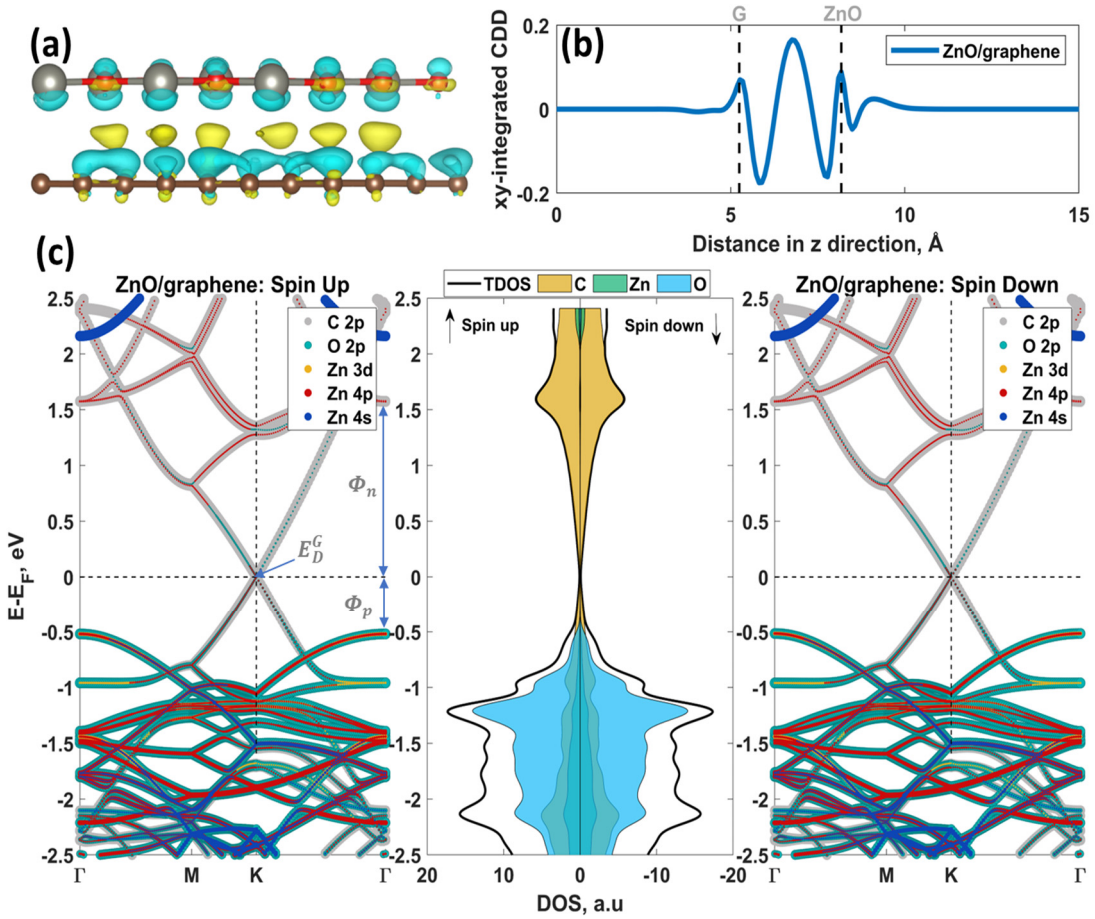


Figure 2. (**a**) Three-dimensional charge density difference plot and (**b**) *x*-*y* plane averaged charge density difference for pristine 2D ZnO/graphene heterostructure. (**c**) Atom- and orbital-projected band structures and PDOS of the spin-up and -down channels for the 2D ZnO/graphene system. The size of each circle corresponds proportionally to the orbital contribution of each band. The Fermi level was set to 0 eV. CDD was estimated as follows: $\Delta\rho = \rho_{2DZnO/graphene} - \rho_{2DZnO} - \rho_{graphene}$. In the case of the 3D-CDD, the isosurface level was set to 0.003, while yellow and cyan colors correspond to positive and negative $\Delta\rho$, respectively.

A careful analysis of the band structure also enabled determining a contact type of the 2DZnO/graphene heterostructure (Figure 2c). According to the Schottky–Mott model [39,40], the *n*-type Schottky barrier Φ_n refers to the difference in energy between the conduction band minimum (CBM) at the high-symmetry point Γ-point and the Fermi level E_F ($\Phi_n = E_{CBM} - E_F$). Likewise, the *p*-type Schottky barrier Φ_p is the difference in energy

between the Fermi level E_F and valence band maximum (VBM) at the high-symmetry point Γ-point ($\Phi_p = E_F - E_{VBM}$). In our case, the values for Φ_n and Φ_p for spin-up/down electrons were determined to be 1.578/1.571 eV and 0.520/0.516 eV, respectively. This result indicates that the 2DZnO/graphene heterostructure has a *p*-type Schottky contact.

It was further revealed that the oxygen vacancies and Fe dopants had a significant effect on the charge transfer between 2D ZnO and graphene, and hence the electronic properties of the combined heterostructure (Figures 3–5). As can be seen from Figure 3a,b, the presence of oxygen vacancies leads to the extension of the charge accumulation region in the middle of the heterostructure. Despite the shape of the CDD curve of the $1V_O$-2D ZnO/graphene structure still resembling that of pristine 2D ZnO/graphene, one can note the emergence of slight asymmetry in the interfacial charge distribution (Figure 3c), with a shift of the central positive peak towards graphene and an increase in the charge depletion near the zinc oxide. Such asymmetry becomes more apparent in the case of the $2V_O$-2DZnO/graphene heterostructure (Figure 3d). Moving to Fe-doped 2D ZnO/graphene heterostructures (Figure 3e–h), it can be concluded that the Fe dopants promote a pronounced charge accumulation from both sides of the graphene, suggesting stronger charge transfer from the 2D ZnO to graphene. This is in good agreement with adhesion analysis results, according to which the adhesion between the Fe-doped 2D ZnO layers and graphene surface is the strongest among all considered structures. Expectedly, the observed peculiarities of the charge distribution at the interfaces containing defects in the zinc oxide layer are reflected in the band structure and PDOS of the investigated heterostructures (Figures 4 and 5). The main observation was the shift of the Dirac point below the Fermi level and the appearance of defect-related energy states near the Fermi level. However, the vdW interaction was confirmed by the well-preserved Dirac cone in graphene, as it was visibly apparent. Table 1 provides a quantitative comparison of the key parameters describing the electronic properties of the heterostructures with a defective 2DZnO layer.

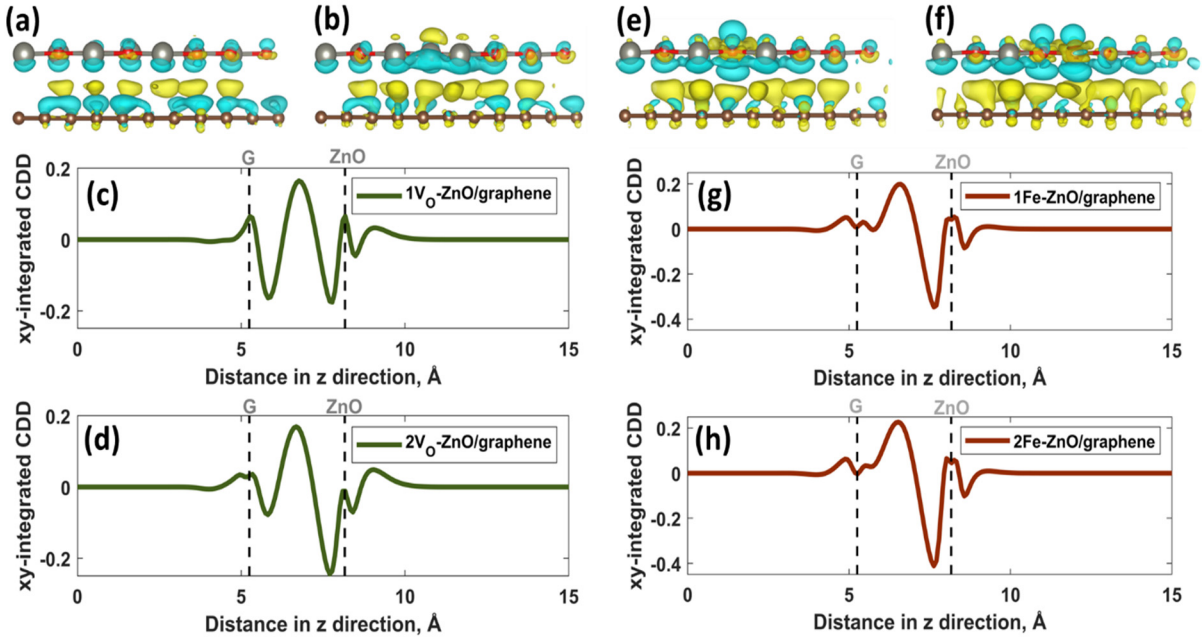


Figure 3. (**a**,**b**) Three-dimensional charge density difference plot and (**c**,**d**) *x*-*y* plane averaged charge density difference for $1V_O$-2DZnO/graphene and $2V_O$-2DZnO/graphene heterostructures, respectively. (**e**,**f**) Three-dimensional charge density difference plot and (**g**,**h**) *x*-*y* plane averaged charge density difference for 1Fe-2DZnO/graphene and 2Fe-2DZnO/graphene heterostructures.

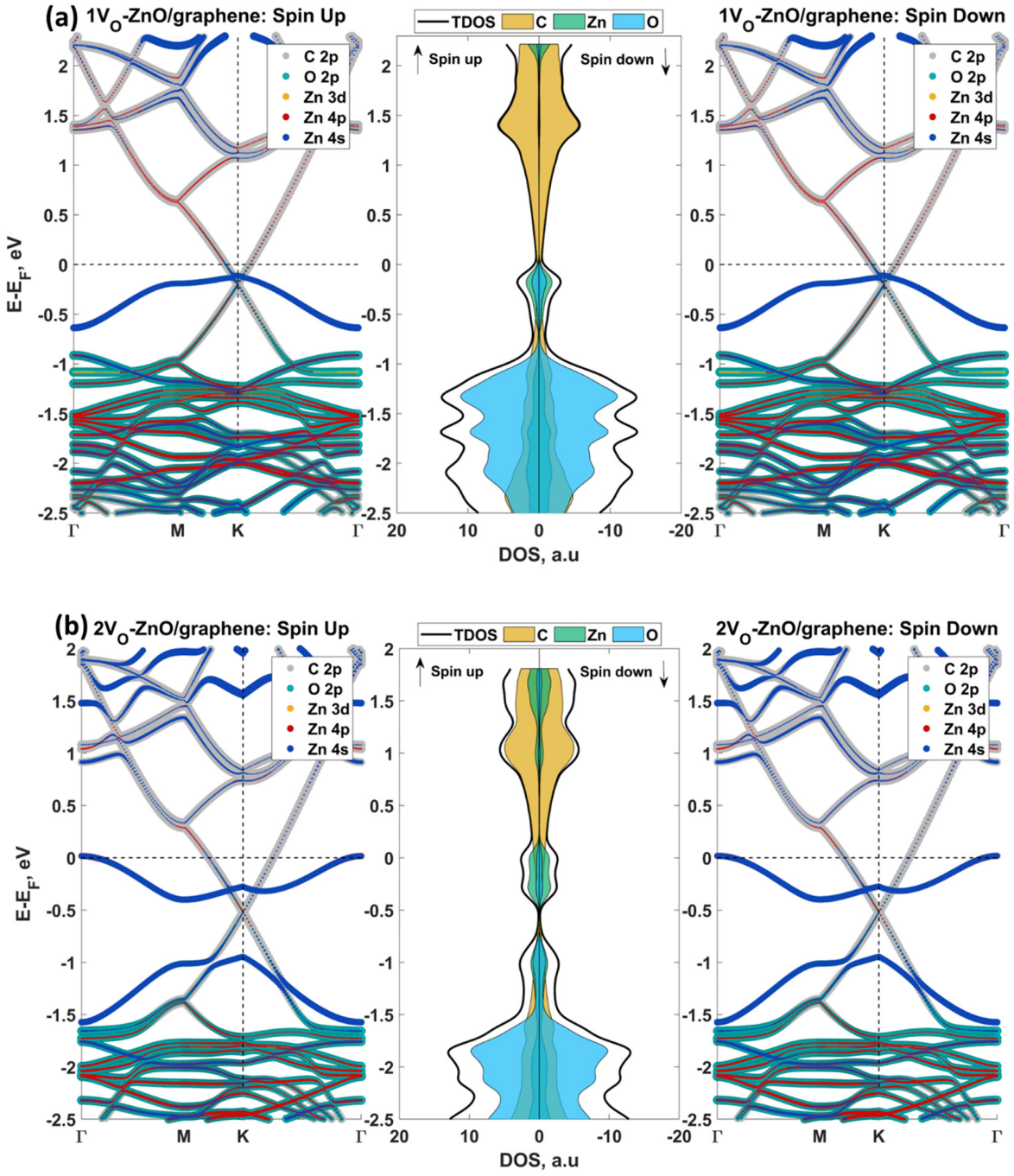


Figure 4. Atom- and orbital-projected band structures and PDOS of the spin-up and -down channels for the (**a**) 1V_O-2DZnO/graphene and (**b**) 2V_O-2DZnO/graphene heterostructures. The size of each circle corresponds proportionally to the orbital contribution of each band.

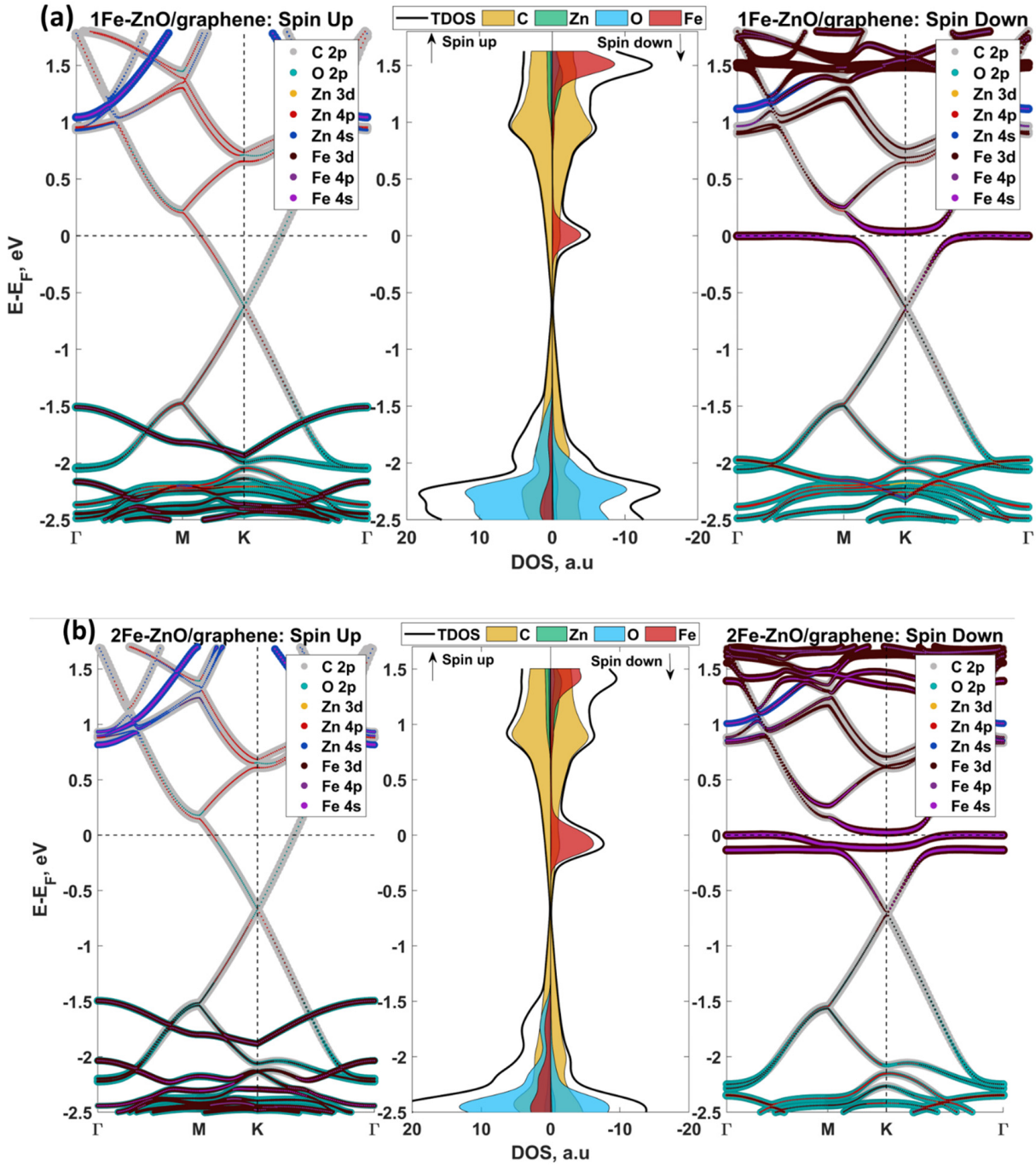


Figure 5. Atom- and orbital-projected band structures and PDOS of the spin-up and -down channels for the (**a**) 1Fe-2DZnO/graphene and (**b**) 2Fe-2DZnO/graphene heterostructures. The size of each circle corresponds proportionally to the orbital contribution of each band.

The analysis of atom- and orbital-projected band structures and PDOS for both the spin-up and -down channels indicates that the occurrence of oxygen vacancies results in the generation of localized defect states in the bandgap of ZnO (Figure 4a,b). These states are inhabited by Zn-4s electrons and predominantly influenced by the proximity of Zn atoms to the oxygen vacancies. One can also notice that the presence of oxygen vacancies in 2D ZnO leads to a shift of both VBM and CBM positions, suggesting the Schottky barrier alteration. In this regard, the $1V_O$-2D ZnO/graphene structure has *p*-type Schottky contact ($\Phi_n < \Phi_p$). On the other hand, the $2V_O$-2D ZnO/graphene heterostructure Φ_p becomes

even more negative (−0.016 eV), suggesting a transition from *p*-type Schottky contact to *p*-type ohmic contact.

Similar to a pristine 2DZnO/graphene heterostructure, the nature of the band structure and PDOS for spin-up and -down channels for vacancy-containing complexes was basically the same. This contrast with the Fe-doped 2DZnO/graphene heterostructures, where the band structures exhibited strong spin polarizations (Figure 5a,b). More specifically, the Dirac point energy of graphene in spin-up and -down directions was approximately −0.619 and −0.643 eV for the 1Fe-2DZnO/graphene heterostructure and −0.663 and −0.691 eV for the 1Fe-2DZnO/graphene heterostructure. Another important observation was that Fe dopants were found to introduce additional states in the ZnO bandgap only in the spin-down direction. Remarkably, the Fe-related defect states were in the close vicinity to the Fermi level. This was probably the main reason for a strong charge transfer between Fe-doped 2D ZnO and graphene.

From Table 1 and Figure 5, it is also seen that there is a pronounced spin-asymmetry of Schottky barriers in Fe-doped 2DZnO/graphene heterostructures. Considering the spin-down channels, it is clear that Φ_p is equal to zero for both 1Fe-2DZnO/graphene and 2Fe-2DZnO/graphene heterostructures, pointing out the *p*-type ohmic behavior of the vdW contacts. Concomitantly, the values of Φ_{n} for the spin-up channels were less than the Φ_{p} values, indicating that an *n*-type Schottky contact was formed in the spin-up direction in the Fe-doped 2DZnO/graphene heterostructures. It is striking to note that the barriers for spin-up holes and electrons differed significantly from each other. Eventually, this may affect the spin-dependent charge transport through the interface [41]. This is referred to as the spin-filter effect [42–44], which arises from the difference in the tunneling rates of electrons/holes with opposite-spin orientations, i.e., spin-up and -down.

To date, this investigation primarily focused on the electronic properties of complex structures. It is justifiable to posit that the formation of these structures entailed reciprocal interactions between zinc oxide and graphene, as exemplified by the previously mentioned displacement of graphene's Dirac point. Nevertheless, in the realm of developing devices based on these heterostructures, the extent of graphene's impact on the band structure of zinc oxide became a pertinent question. To address this, additional calculations with a specific emphasis on free-standing ZnO monolayers were conducted. The band structures of free-standing monolayers of zinc oxide are presented in Figures S6–S11 (Supplementary Material). Overall, these findings demonstrate a qualitative agreement with the results obtained for zinc oxide monolayers supported by graphene. Specifically, the conduction band of pristine 2D ZnO primarily consists of Zn 4*s* states, while the valence band is predominantly dominated by O 2*p* states, with a reduced contribution from Zn-related states (Figure S6, Supplementary Material). However, the presence of oxygen vacancies leads to the formation of localized Zn 4s states above the valence band maximum, which is primarily composed of O 2*p* states (Figures S7 and S8, Supplementary Material).

Turning our attention to free-standing monolayers of zinc oxide doped with iron (Figures S9 and S10, Supplementary Material), there was a noticeable tendency for the emergence of Fe-doped electronic states in close proximity to the Fermi level, albeit only in the spin-down direction. Furthermore, through a comprehensive comparative analysis of the band structures of zinc oxide monolayers in the presence and absence of graphene (Figures S11–S15, Supplementary Material), several significant observations were made. Firstly, the presence of graphene induced an upward shift of the valence band maximum and conduction band minimum for both pristine 2D ZnO and $2V_O$-2D ZnO systems. Secondly, an actual narrowing of the band gap occurred in the $1V_O$-2D ZnO system. Lastly, systems containing iron exhibited a shift of Fe-related states closer to the Fermi level. These distinct characteristics can be directly attributed to the interfacial charge transfer occurring between the ZnO monolayer and graphene.

Bearing in mind that the defects can induce magnetism in the otherwise non-magnetic ZnO material, it would be interesting to find out whether there was an effect of the oxygen vacancies and Fe dopants on the spin-density distribution in the 2D ZnO/graphene

heterostructure. For this purpose, the spin density determined as a difference between the spin-α (spin-up) and spin-β (spin-down) densities was predicted for all considered heterostructures (Figure 6). Before proceeding to the discussion of the results, it is important to emphasize that neutral oxygen vacancies were not expected to introduce additional magnetic moments in the 2D ZnO. This is because they have spin-zero ground states in ZnO [45]. On the other hand, Fe doping of ZnO is a common strategy to achieve a high spin density in ZnO-based materials [46–48]. In this regard, as opposed to very low spin densities for pristine and V_O-containing systems displayed with an isosurface value of 10^{-5}, high spin densities demonstrated for Fe-containing systems are represented by isosurfaces corresponding to 0.001. The spin density plots for pristine 2D ZnO/graphene and $1V_O$-2D ZnO/graphene heterostructures show the spin density is localized entirely in all oxygen atoms (Figure 6a,b), while, for the ZnO/graphene heterostructure, the spin density is additionally redistributed around the oxygen vacancy sites (Figure 6c). A completely different picture appears in the presence of Fe dopants (Figure 6d,e). Particularly, spin density is mainly localized on the Fe atoms and their adjacent oxygen neighbors, indicating the formation of localized magnetic moments within the ZnO nanosheet due to the presence of Fe atoms. Furthermore, spin-density localization was even observed on the carbon atoms of graphene. This underlines the critically important role of Fe dopants in inducing the magnetism in the 2D ZnO/graphene vdW heterostructure.

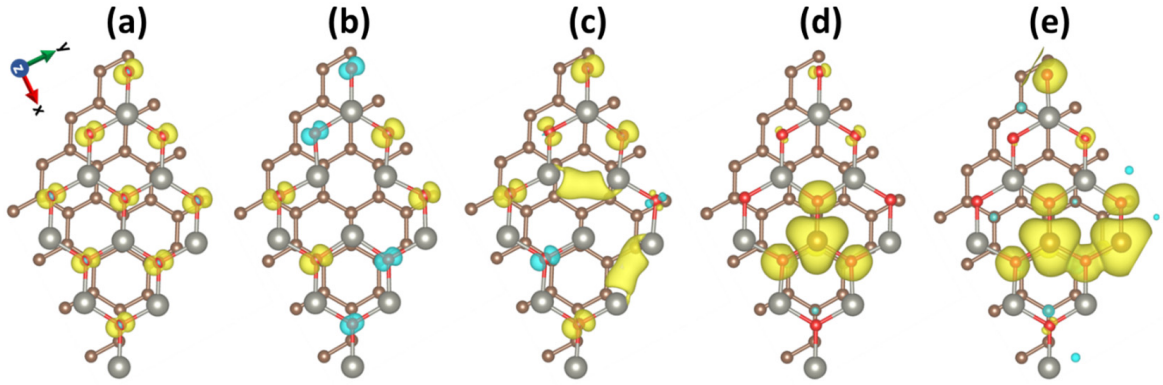


Figure 6. Spin-density distribution plot of (**a**) pristine 2D ZnO/graphene, (**b**) $1V_O$-2DZnO/graphene, (**c**) $2V_O$-2DZnO/graphene, (**d**) 1Fe-2DZnO/graphene, and (**c**) 2Fe-2DZnO/graphene heterostructures. For (**a**–**c**), the isosurface level is set to 10^{-5} a.u., while for (**d**,**e**), the isosurface corresponds to 0.001 a.u.

3.3. Hydrogen-Adsorption Properties

The changes in electronic properties induced by oxygen vacancies and Fe dopants were expected to enhance the sensitivity and catalytic activity of the 2D ZnO/graphene system, making it a promising material for sensing and catalytic applications. To verify this, hydrogen adsorption—the Volmer step of the hydrogen evolution reaction—onto pristine and defective 2D ZnO/graphene heterostructures was investigated as a model chemical process. The focus was on estimating the free energy of hydrogen adsorption (ΔG_{H^*}), which is believed to be an essential factor describing the HER performance of catalysts. To accomplish this, the value of ΔG_{H^*} was computed using the following equation: $\Delta G_{H^*} = \Delta E_{H^*} + 0.24$ eV. Here, ΔE_{H^*} represents the hydrogen-adsorption energy, whereas the term 0.24 eV accounts for the changes in entropy and zero-point energy (ZPE) between gaseous and absorbed hydrogen. All possible adsorption sites were checked (please see Figure 7a, where the numbers designate the considered zinc and oxygen sites). The heatmaps presented in Figure 7b,c suggest that the hydrogen-adsorption energy is strongly influenced by the nature of the adsorption site of the pristine 2D ZnO/graphene heterostructure, with the oxygen sites exhibiting greater adsorption energy compared to the zinc sites. Oxygen sites bind to hydrogen atoms more strongly than zinc ones because of the difference in their electronegativities. Whereas the highly electronegative oxygen has a

strong ability to attract electrons to form a strong polar covalent bond, the relatively low electronegativity of zinc dictates its much weaker interaction with hydrogen. However, the ΔG_{H^*} values for both adsorption site types were negative, indicating that this process was thermodynamically favorable. Notably, even chemically similar sites (zinc or oxygen sites) had different binding abilities. This was driven by the charge transfer between 2D ZnO and graphene, which brings the site-energy inhomogeneity to the system. It is of utmost importance to highlight that the presence of graphene plays a pivotal role in facilitating charge transfer at the interface. This becomes evident when examining the hydrogen-adsorption behavior in the absence of graphene, resulting in ΔG_{H^*} becoming more negative for hydrogen adsorption at Zn sites and less negative for hydrogen adsorption at O sites, as depicted in Figure S16 (Supplementary Material). This finding not only highlights graphene's crucial function as a stabilizing and supportive substrate, but also underscores its influence on hydrogen adsorption. Figure 7d,e exhibit the dependence of hydrogen-adsorption energy for zinc and oxygen sites on hydrogen coverage. The results indicate that the hydrogen-adsorption energy for zinc sites becomes more negative with increasing hydrogen coverage, which may be indicative of negligibly small repulsive interactions between the hydrogen species. This is achieved through a 2D ZnO structure transformation from a flat to buckled geometry during the H-adsorption process and a formation of tilted chemical Zn–H bonds (see the inset of Figure 7d). Despite the 2D ZnO layer reconstruction upon H adsorption, no significant atomic fluctuations in the *z* direction for oxygen and zinc sublayers were observed. These findings have important implications for the development of efficient hydrogen storage materials based on 2D ZnO/graphene systems. On the other hand, the ΔG_{H^*} value for oxygen sites became less negative with increasing the hydrogen coverage (Figure 7e). Furthermore, the hydrogen adsorption induced the significant deformation/corrugation of the 2D ZnO layer (please see the inset of Figure 7e). The geometry optimization in full-coverage conditions did not converge correctly. For this reason, in this work, only low and moderate hydrogen-coverage conditions on O-sites of 2D ZnO were considered. While the absence of graphene had minimal impact on the relationship between ΔG_{H^*} and hydrogen coverage on Zn sites (left panel, Figure S17, Supplementary Material), it significantly altered the trend for oxygen sites. Specifically, it was observed that the absolute value of ΔG_{H^*} tended to increase as the hydrogen coverage at oxygen sites increased (right panel, Figure S17, Supplementary Material).

The comparison of ΔG_{H^*} heatmaps for defect-engineered 2DZnO/graphene heterostructures enables us to understand the effect of oxygen vacancies and Fe dopants on hydrogen adsorption (Figure 8). The adsorption energies of zinc sites adjacent to oxygen vacancy sites on V_O-containing surfaces (Figure 8a,b) were much stronger compared to those on the pristine 2D ZnO surface. When discussing Fe-doped systems (Figure 8c,d), it is observed that H-adsorption energies are significantly stronger at Fe sites than Zn sites, resulting in preferential H adsorption at Fe sites over Zn sites. Notably, for surfaces with one Fe substitutional defect (Figure 8c), Zn sites next to an Fe site (labeled as 1 and 9) have much lower ΔG_{H^*} values than neighboring Fe and Zn sites, implying that H can preferentially bind at Zn sites adjacent to Fe. However, for the surface where two Fe sites are incorporated into 2D ZnO (Figure 8d), the situation is different. Although Fe sites still exhibit significantly higher ΔG_{H^*} values, the Gibbs free energy of hydrogen-adsorption energies becomes considerably stronger at all Zn sites than those of the 1Fe-doped 2D ZnO system. This suggests that the distance between Fe dopants in 2D ZnO can significantly affect the HER performance of 2DZnO/graphene heterogeneous catalysts. It is important to note that the ΔG_{H^*} value should approach zero for an ideal catalyst, and systems with isolated Fe substitutional defects appear to be more promising for HER catalysis, requiring careful further investigation.

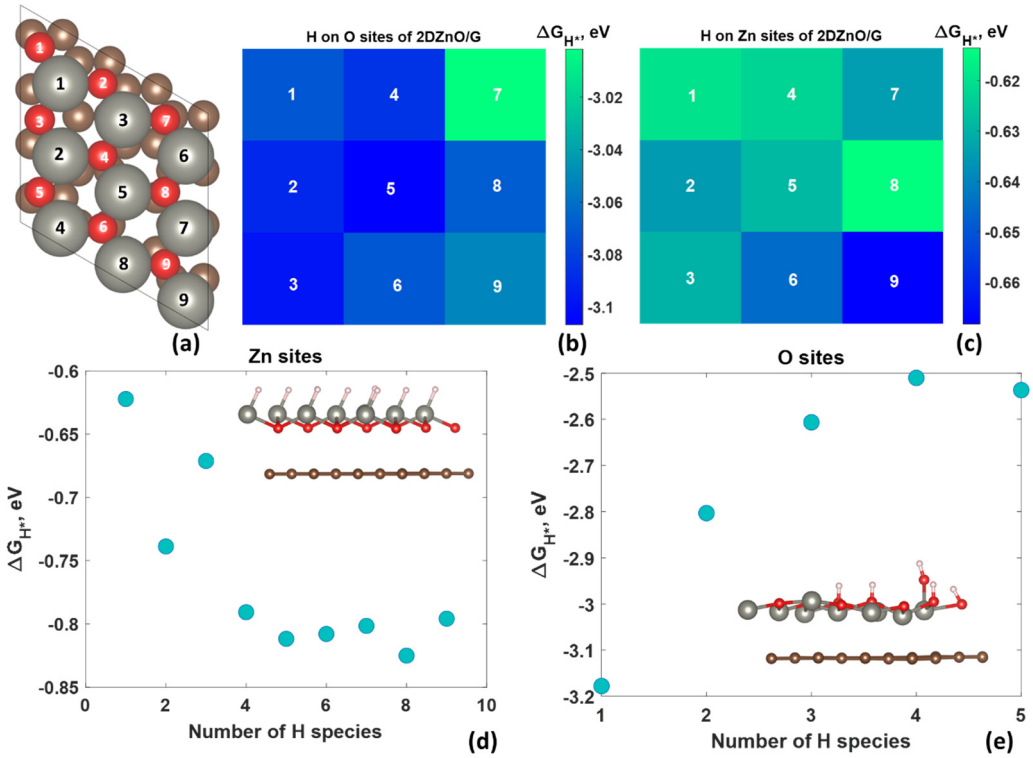


Figure 7. Panel (**a**) displays the oxygen- and zinc-adsorption sites for the 2D ZnO/graphene heterostructure and the sequence in which they become occupied by hydrogen species. Heatmaps of predicted Gibbs free energy of adsorption, ΔG_{H^*}, for the Volmer step on oxygen- (**b**) and zinc (**c**) adsorption sites of 2DZnO/graphene. Dependence of hydrogen-adsorption energy on hydrogen coverage for (**d**) Zn and (**e**) O sites of 2DZnO/graphene. The insets demonstrate the optimized geometrical configurations of 2DZnO/graphene with maximum acceptable H coverage for both Zn and O sites.

Figure S18 (Supplementary Material) illustrates the impact of oxygen vacancies and Fe dopants on ΔG_{H^*} values for hydrogen adsorption at different oxygen sites within the studied structures. The introduction of oxygen vacancies generally results in an increase in the absolute value of ΔG_{H^*}, indicating enhanced hydrogen adsorption at the remaining oxygen sites. This effect was particularly pronounced in the 1Vo-ZnO/graphene structure, as evidenced by the more negative ΔG_{H^*} values observed for specific oxygen sites. Conversely, the incorporation of Fe dopants in the ZnO/graphene structure led to a decrease in the absolute value of ΔG_{H^*} at oxygen sites compared to the pristine structure. The influence of Fe dopants becomes more intricate in the case of 2Fe-ZnO/graphene, with some sites showing reduced adsorption energies (approximately -0.57 eV and -1.42 eV), while others exhibit more negative ΔG_{H^*} values (≥ -2.4 eV). These findings highlight the diverse effects of Fe dopants on hydrogen-adsorption properties within the heterostructures, indicating site-dependent variations in the catalytic activity. To shed more light on the nature of the site-dependent properties, the Hirshfeld population analysis was performed. There was a correlation between the charge at oxygen sites and the ΔG_{H^*} values for hydrogen adsorption. In the case of oxygen vacancies, the introduction of a vacancy disrupted the balance of charge within the system (Figure S19, Supplementary Material), leading to an increase in the negative charge at neighboring oxygen sites. This increased negative charge on the remaining oxygen atoms can enhance the electrostatic attraction with neutral hydrogen, resulting in a more negative ΔG_{H^*} and enhanced hydrogen adsorption. This is consistent with the trend observed in the 1Vo-ZnO/graphene structure, where specific oxygen sites exhibit more negative ΔG_{H^*} values, indicating stronger hydrogen binding due to the increased negative charge at these sites. Conversely, the incorporation of Fe

dopants reduced the negative charge at the oxygen sites compared to the pristine structure (Figure S19, Supplementary Material). As a result, the electrostatic attraction between oxygen and hydrogen can weaken, leading to a decrease in the absolute value of ΔG_{H^*} and indicating a weaker binding of hydrogen. The observed trends support the notion that the charge distribution, influenced by the presence of oxygen vacancies and Fe dopants, plays a crucial role in modulating the strength of hydrogen binding and catalytic activity within the heterostructures.

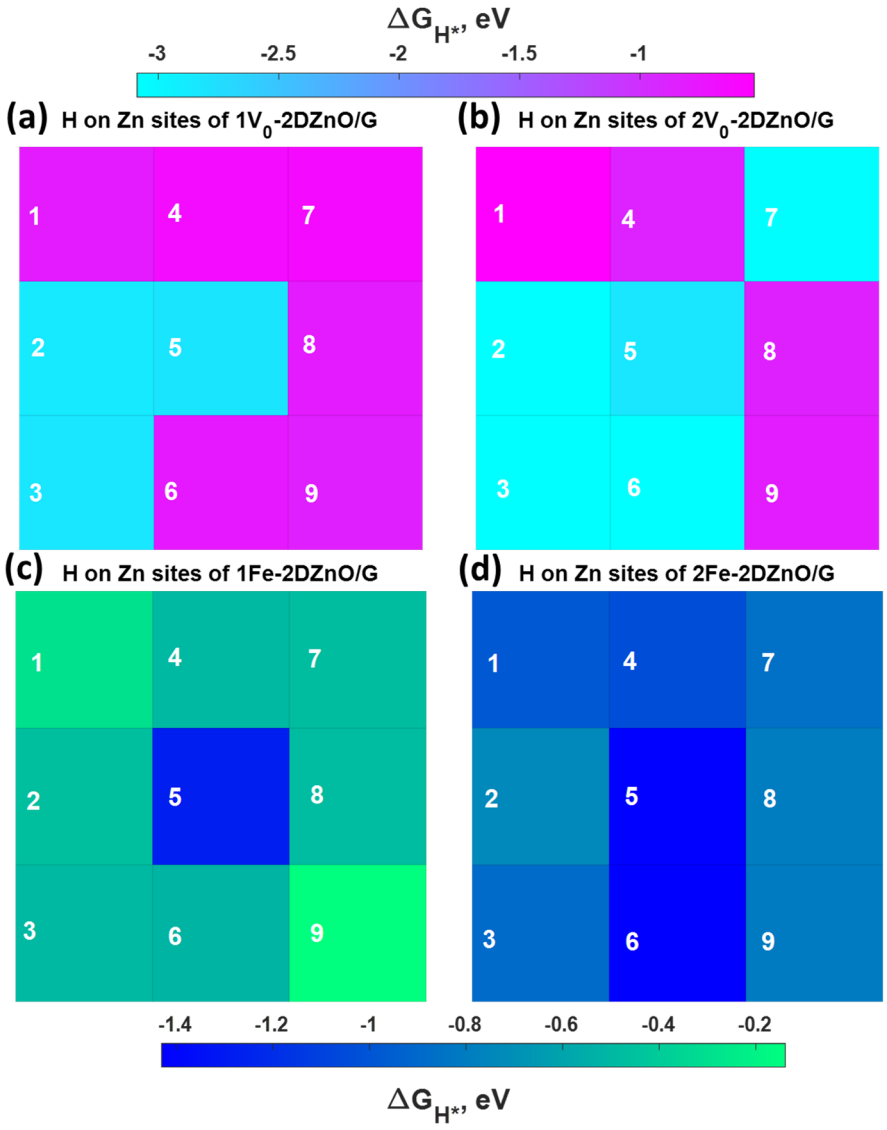


Figure 8. Heatmaps of predicted Gibbs free energy of adsorption, ΔG_{H^*}, for the Volmer step on zinc-adsorption sites of defect-engineered 2DZnO/graphene heterostructure: (**a**,**b**) oxygen vacancies and (**c**,**d**) Fe dopants, respectively.

Upon analyzing the data obtained from free-standing defect-engineered ZnO monolayers, notable trends emerge. Firstly, for the Zn sites adjacent to oxygen vacancy sites in vacancy-containing systems, the presence of graphene leads to more negative values of ΔG_{H^*} compared to its absence (Figure S20, Supplementary Material). Conversely, for other Zn sites in systems without graphene, ΔG_{H^*} becomes even less negative. These observations suggest that the presence of graphene not only enhances hydrogen adsorption at specific Zn sites, but also amplifies the heterogeneity in the adsorption behavior of Zn sites. In contrast, for all O sites, the values of ΔG_{H^*} exhibited greater negativity in the

presence of graphene. This indicates that graphene contributes to an increased stability and stronger binding of hydrogen at oxygen sites. The enhanced negative values of ΔG_{H^*} further underscore the influence of graphene in facilitating hydrogen adsorption at the oxygen sites. Iron-containing systems exhibit two distinct and contrasting trends (Figure S21, Supplementary Material): the presence of graphene substantially reduces the absolute value of ΔG_{H^*} for hydrogen adsorption at Zn sites, while simultaneously augmenting the adsorption capacity of O sites, thereby promoting a stronger affinity between hydrogen atoms and the substrate.

4. Conclusions

In this study, the effects of different types of defects on the properties of 2D ZnO supported by graphene were investigated using GGA-PBE+U-D2 calculations. It was found that significant changes in the heterostructure properties, such as the alteration of the interlayer adhesion strength, the creation of mid-gap states and the modulation of the electronic band structure, and catalytic activity, were caused by the formation of defects. The alteration of not only the magnitude, but also the nature of the Schottky barrier, could be affected by the formation of defects in the 2D ZnO layer of the heterostructure. The transition from the *p*-type Schottky barrier to *p*-type ohmic behavior of the vdW contacts was identified when introducing Fe_{Zn} substitutional defects into the system. The adsorption energy of hydrogen on pristine 2DZnO/graphene was strongly influenced by the adsorption site, with a higher adsorption energy observed at oxygen sites than at zinc sites. Site energy inhomogeneity created by the charge transfer between 2D ZnO and graphene affected the hydrogen-adsorption energy. Zinc sites exhibited more negative hydrogen-adsorption energy with increasing hydrogen coverage, indicating negligibly lower repulsive interactions between the hydrogen species. Significantly larger ΔG_{H^*} values were observed at Fe sites compared to Zn sites, and the HER performance of 2DZnO/graphene heterogeneous catalysts could be significantly affected by the distance between Fe dopants in 2D ZnO.

This study brings to light the substantial influence of graphene on the electronic properties and adsorption characteristics within 2D ZnO/graphene heterostructures. These findings underscore the critical role of defect engineering in tailoring the properties of graphene-supported 2D ZnO, thus enabling advancements in efficient hydrogen storage materials and catalytic hydrogen evolution reactions (HER) based on 2D ZnO/graphene systems.

Supplementary Materials: The following supporting information can be downloaded at: https://www.mdpi.com/article/10.3390/app13127243/s1, Table S1: A comparison of adhesion energies predicted at different convergence tolerances; Figure S1: Band structure and PDOS of the spin up and spin down channels for the pristine 2DZnO/graphene heterostructure, predicted at different convergence tolerance: 0.01eV/Å and 0.02eV/Å, respectively; Figure S2: Band structure and PDOS of the spin up and spin down channels for the $1V_O$-2DZnO/graphene heterostructure, predicted at different convergence tolerance: 0.01eV/Å and 0.02eV/Å, respectively.; Figure S3: Band structure and PDOS of the spin up and spin down channels for the $2V_O$-2DZnO/graphene heterostructure, predicted at different convergence tolerance: 0.01eV/Å and 0.02eV/Å, respectively; Figure S4: Band structure and PDOS of the spin up and spin down channels for the 1Fe-2DZnO/graphene heterostructure, predicted at different convergence tolerance: 0.01eV/Å and 0.02eV/Å, respectively; Figure S5: Band structure and PDOS of the spin up and spin down channels for the 2Fe-2DZnO/graphene heterostructure, predicted at different convergence tolerance: 0.01eV/Å and 0.02eV/Å, respectively; Table S2: A comparison of *z* coordinates of carbon atoms belonging to graphene in different 2DZnO/G systems; Figure S6: Band structure and PDOS of the spin up and spin down channels for the free-standing pristine 2DZnO. The size of each circle corresponds proportionally to the orbital contribution of each band; Figure S7: Band structure and PDOS of the spin up and spin down channels for the free-standing $1V_O$-2DZnO. The size of each circle corresponds proportionally to the orbital contribution of each band; Figure S8: Band structure and PDOS of the spin up and spin down channels for the free-standing $2V_O$-2DZnO. The size of each circle corresponds proportionally to the orbital

contribution of each band; Figure S9: Band structure and PDOS of the spin up and spin down channels for the free-standing 1Fe-2DZnO. The size of each circle corresponds proportionally to the orbital contribution of each band; Figure S10: Fat band structure and PDOS of the spin up and spin down channels for the free-standing 2Fe-2DZnO. The size of each circle corresponds proportionally to the orbital contribution of each band; Figure S11: Band structure and PDOS of the spin up and spin down channels for the free-standing pristine 2DZnO, predicted with and without graphene; Figure S12: Band structure and PDOS of the spin up and spin down channels for the free-standing $1V_O$-2DZnO, predicted with and without graphene; Figure S13: Band structure and PDOS of the spin up and spin down channels for the free-standing $2V_O$-2DZnO, predicted with and without graphene; Figure S14: Band structure and PDOS of the spin up and spin down channels for the free-standing 1Fe-2DZnO, predicted with and without graphene; Figure S15: Fat band structure and PDOS of the spin up and spin down channels for the free-standing 2Fe-2DZnO, predicted with and without graphene; Figure S16: ΔG_{H^*} variations on zinc (left panel) and oxygen (right panel) adsorption sites of 2DZnO in the presence and the absence of graphene (G), respectively; Figure S17: Dependence of the hydrogen adsorption energy on hydrogen coverage for (left panel) Zn sites and (right panel) O sites of free-standing 2DZnO, respectively; Figure S18: Gibbs free energy of adsorption, ΔG_{H^*}, for the Volmer step on oxygen adsorption sites of pristine and defect-engineered 2DZnO/graphene heterostructures; Figure S19: Hirshfeld charge variations on oxygen adsorption sites of pristine and defect-engineered 2DZnO/graphene heterostructures; Figure S20: ΔG_{H^*} variations on vacancy-containing 2DZnO in the presence and the absence of graphene (G): (a) Zn sites at $1V_O$-2D ZnO, (b) O sites at $1V_O$-2D ZnO, (c) Zn sites at $2V_O$-2D ZnO, (d) O sites at $2V_O$-2D ZnO, respectively; Figure S21: ΔG_{H^*} variations on Fe-doped 2DZnO in the presence and the absence of graphene (G): (a) Zn sites at 1Fe-2D ZnO, (b) O sites at 1Fe-2D ZnO, (c) Zn sites at 2Fe-2D ZnO and (d) O sites at 2Fe-2D ZnO, respectively.

Funding: This research was funded by the ÅForsk Foundation, Grant 21–112.

Institutional Review Board Statement: Not applicable.

Informed Consent Statement: Not applicable.

Data Availability Statement: The data that support the findings of this study are available within the article.

Acknowledgments: The computations and data handling were enabled by resources provided by the National Supercomputer Centre (NSC), funded by Linköping University.

Conflicts of Interest: The author declares no conflict of interest.

References

1. Son, S.; Cho, Y.; Hong, H.-K.; Lee, J.; Kim, J.H.; Kim, K.; Lee, Y.; Yoon, A.; Shin, H.-J.; Lee, Z. Spontaneous Formation of a ZnO Monolayer by the Redox Reaction of Zn on Graphene Oxide. *ACS Appl. Mater. Interfaces* **2020**, *12*, 54222–54229. [CrossRef] [PubMed]
2. Fabris, G.S.L.; Marana, N.L.; Laranjeira, J.A.S.; Longo, E.; Sambrano, J.R. New Two-Dimensional Zinc Oxide Nanosheets: Properties, Stability, and Interconversion. *Mater. Lett.* **2020**, *275*, 128067. [CrossRef]
3. Wang, J.; Yang, H.; Yang, P. Photoelectric Properties of 2D ZnO, Graphene, Silicene Materials and Their Heterostructures. *Compos. Part B* **2022**, *233*, 109645. [CrossRef]
4. Peng, Q.; Liang, C.; Ji, W.; De, S. A First Principles Investigation of the Mechanical Properties of g-ZnO: The Graphene-like Hexagonal Zinc Oxide Monolayer. *Comput. Mater. Sci.* **2013**, *68*, 320–324. [CrossRef]
5. Rahimi, K. Tunable Electronic Properties of the Novel g-ZnO/1T-TiS2 vdW Heterostructure by Electric Field and Strain: Crossovers in Bandgap and Band Alignment Types. *Phys. Chem. Chem. Phys.* **2020**, *22*, 7412–7420. [CrossRef]
6. Sikam, P.; Takahashi, K.; Roongcharoen, T.; Jitwatanasirikul, T.; Chitpakdee, C.; Faungnawakij, K.; Namuangruk, S. Effect of 3d-Transition Metals Doped in ZnO Monolayers on the CO_2 Electrochemical Reduction to Valuable Products: First Principles Study. *Appl. Surf. Sci.* **2021**, *550*, 149380. [CrossRef]
7. Ta, H.Q.; Zhao, L.; Pohl, D.; Pang, J.; Trzebicka, B.; Rellinghaus, B.; Pribat, D.; Gemming, T.; Liu, Z.; Bachmatiuk, A.; et al. Graphene-Like ZnO: A Mini Review. *Crystals* **2016**, *6*, 100. [CrossRef]
8. Luo, X.; Wang, G.; Huang, Y.; Wang, B.; Yuan, H.; Chen, H. Bandgap Engineering of the g-ZnO Nanosheet via Cationic-Anionic Passivated Codoping for Visible-Light-Driven Photocatalysis. *J. Phys. Chem. C* **2017**, *121*, 18534–18543. [CrossRef]
9. Leonardi, S.G. Two-Dimensional Zinc Oxide Nanostructures for Gas Sensor Applications. *Chemosensors* **2017**, *5*, 17. [CrossRef]
10. Krishna, M.S.; Singh, S.; Batool, M.; Fahmy, H.M.; Seku, K.; Shalan, A.E.; Lanceros-Mendez, S.; Zafar, M.N. A review on 2D-ZnO nanostructure based biosensors: From materials to devices. *Mater. Adv.* **2023**, *4*, 320–354. [CrossRef]

11. Napi, M.L.M.; Sultan, S.M.; Ismail, R.; How, K.W.; Ahmad, M.K. Electrochemical-Based Biosensors on Different Zinc Oxide Nanostructures: A Review. *Materials* **2019**, *12*, 2985. [CrossRef]
12. Sahoo, T.; Nayak, S.K.; Chelliah, P.; Rath, M.K.; Parida, B. Observations of Two-Dimensional Monolayer Zinc Oxide. *Mater. Res. Bull.* **2016**, *75*, 134–138. [CrossRef]
13. Hong, H.-K.; Jo, J.; Hwang, D.; Lee, J.; Kim, N.Y.; Son, S.; Kim, J.H.; Jin, M.-J.; Jun, Y.C.; Erni, R.; et al. Atomic Scale Study on Growth and Heteroepitaxy of ZnO Monolayer on Graphene. *Nano Lett.* **2017**, *17*, 120–127. [CrossRef]
14. Chen, L.; Cui, Y.; Xiong, Z.; Zhou, M.; Gao, Y. Chemical Functionalization of the ZnO Monolayer: Structural and Electronic Properties. *RSC Adv.* **2019**, *9*, 21831–21843. [CrossRef]
15. Zhou, Q.; Zhang, G.; Tian, S.; Zhang, X. First-Principles Insight into Pd-Doped ZnO Monolayers as a Promising Scavenger for Dissolved Gas Analysis in Transformer Oil. *ACS Omega* **2020**, *5*, 17801–17807. [CrossRef]
16. Ekuma, C.E.; Najmaei, S. Graphene/ZnO van der Waals Stacks for Thermal Management. *ACS Appl. Nano Mater.* **2020**, *3*, 7136–7142. [CrossRef]
17. Sahatiya, P.; Jones, S.S.; Gomathi, P.T.; Badhulika, S. Flexible substrate based 2D ZnO (n)/graphene (p) rectifying junction as enhanced broadband photodetector using strain modulation. *2D Mater.* **2017**, *4*, 025053. [CrossRef]
18. Marfoua, B.; Hong, J. Graphene Induced High Thermoelectric Performance in ZnO/Graphene Heterostructure. *Adv. Mater. Interfaces* **2023**, *10*, 2202387. [CrossRef]
19. Zhang, H.; Lv, R. Defect engineering of two-dimensional materials for efficient electrocatalysis. *J. Mater.* **2018**, *4*, 95–107. [CrossRef]
20. Liu, F.; Fan, Z. Defect engineering of two-dimensional materials for advanced energy conversion and storage. *Chem. Soc. Rev.* **2023**, *52*, 1723–1772. [CrossRef]
21. Chen, H.; Qu, Y.; Ding, J.; Fu, H. Adsorption behavior of graphene-like ZnO monolayer with oxygen vacancy defects for NO2: A DFT study. *Superlattices Microstruct.* **2019**, *134*, 106223. [CrossRef]
22. Yang, R.; Du, Y. Adsorption and dissociation of a single water molecule on graphene-like ZnO monolayer with oxygen vacancies: A first-principles study. *Phys. Scr.* **2023**, *98*, 035826. [CrossRef]
23. Yao, Q.; Liu, Y.; Lu, R.; Xiao, C.; Deng, K.; Kan, E. Will a graphitic-like ZnO single-layer be an ideal substrate for graphene? *RSC Adv.* **2014**, *4*, 17478–17482. [CrossRef]
24. Liu, Y.; Yang, X. Effects of Fe doping on the magnetic and absorption spectrum of graphene-like ZnO monolayer from first-principles calculations. *Chem. Phys.* **2023**, *565*, 111742. [CrossRef]
25. Ghorbanzadeh Ahangari, M.; Mashhadzadeh, A.H.; Fathalian, M.; Dadrasi, A.; Rostamiyan, Y.; Mallahi, A. Effect of various defects on mechanical and electronic properties of zinc-oxide graphene-like structure: A DFT study. *Vacuum* **2019**, *165*, 26–34. [CrossRef]
26. Soler, J.M.; Artacho, E.; Gale, J.D.; García, A.; Junquera, J.; Ordejón, P.; Sánchez-Portal, D.T. The SIESTA method for ab initio order-N materials simulation. *J. Phys. Condens. Matter* **2002**, *14*, 2745–2779. [CrossRef]
27. Perdew, J.P.; Burke, K.; Ernzerhof, M. Generalized Gradient Approximation Made Simple. *Phys. Rev. Lett.* **1996**, *77*, 3865. [CrossRef]
28. Grimme, S. Semiempirical GGA-type density functional constructed with a long-range dispersion correction. *J. Comput. Chem.* **2006**, *27*, 1787–1799. [CrossRef]
29. Bashyal, K.; Pyles, C.K.; Afroosheh, S.; Lamichhane, A.; Zayak, A.T. Empirical optimization of DFT + U and HSE for the band structure of ZnO. *J. Phys. Condens. Matter* **2018**, *30*, 065501. [CrossRef]
30. Dudarev, S.L.; Botton, G.A.; Savrasov, S.Y.; Humphreys, C.J.; Sutton, A.P. Electron-energy-loss spectra and the structural stability of nickel oxide: An LSDA+U study. *Phys. Rev. B* **1998**, *57*, 1505. [CrossRef]
31. Wu, H.-C.; Peng, Y.-C.; Shen, T.-P. Electronic and Optical Properties of Substitutional and Interstitial Si-Doped ZnO. *Materials* **2012**, *5*, 2088–2100. [CrossRef]
32. Shtepliuk, I.; Yakimova, R. Interaction of H and Li with epitaxial graphene on SiC: A comparative analysis by first principles study. *Appl. Surf. Sci.* **2021**, *568*, 150988. [CrossRef]
33. Shtepliuk, I.; Yakimova, R. Computational Appraisal of Silver Nanocluster Evolution on Epitaxial Graphene: Implications for CO Sensing. *ACS Omega* **2021**, *6*, 38, 24739–24751. [CrossRef]
34. Shtepliuk, I.; Ivanov, I.G.; Pliatsikas, N.; Iakimov, T.; Lara-Avila, S.; Ho Kim, K.; Ben Sedrine, N.; Kubatkin, S.E.; Sarakinos, K.; Yakimova, R. Clustering and Morphology Evolution of Gold on Nanostructured Surfaces of Silicon Carbide: Implications for Catalysis and Sensing. *ACS Appl. Nano Mater.* **2021**, *4*, 1282–1293. [CrossRef]
35. Shtepliuk, I.; Vagin, M.; Khan, Z.; Zakharov, A.A.; Iakimov, T.; Giannazzo, F.; Ivanov, I.G.; Yakimova, R. Understanding of the Electrochemical Behavior of Lithium at Bilayer-Patched Epitaxial Graphene/4H-SiC. *Nanomaterials* **2022**, *12*, 2229. [CrossRef]
36. Available online: https://departments.icmab.es/leem/siesta/Pseudopotentials/ (accessed on 2 May 2023).
37. Nørskov, J.K.; Bligaard, T.; Logadottir, A.; Kitchin, J.R.; Chen, J.G.; Pandelov, S.; Stimming, U. Trends in the Exchange Current for Hydrogen Evolution. *J. Electrochem. Soc.* **2005**, *152*, J23–J26. [CrossRef]
38. Gong, A.; Feng, Y.; Liu, C.; Chen, J.; Wang, Z.; Shen, T. A promising ZnO/Graphene van der Waals heterojunction as solar cell devices: A first-principles study. *Energy Rep.* **2022**, *8*, 904–910. [CrossRef]
39. Tung, R.T. The physics and chemistry of the Schottky barrier height. *Appl. Phys. Rev.* **2014**, *1*, 011304. [CrossRef]
40. Liu, Y.; Guo, J.; Zhu, E.; Liao, L.; Lee, S.-J.; Ding, M.; Shakir, I.; Gambin, V.; Huang, Y.; Duan, X. Approaching the Schottky–Mott Limit in van der Waals Metal–Semiconductor Junctions. *Nature* **2018**, *557*, 696–700. [CrossRef]

41. Li, H.; Xu, Y.-K.; Cheng, Z.-P.; He, B.-G.; Zhang, W.-B. Spin-Dependent Schottky Barriers and Vacancy Induced Spin-Selective Ohmic Contacts in Magnetic vdW Heterostructures. *Phys. Chem. Chem. Phys.* **2020**, *22*, 9460. [CrossRef]
42. Klein, D.R.; MacNeill, D.; Lado, J.L.; Soriano, D.; Navarro-Moratalla, E.; Watanabe, K.; Taniguchi, T.; Manni, S.; Canfield, P.; Fernández-Rossier, J.; et al. Magnetic Field Effect in Electrostatically Doped Twisted Graphene/hBN/Graphene Trilayers. *Science* **2018**, *360*, 1218–1222. [CrossRef] [PubMed]
43. Song, T.; Cai, X.; Tu, M.W.-Y.; Zhang, X.; Huang, B.; Wilson, N.P.; Seyler, K.L.; Zhu, L.; Taniguchi, T.; Watanabe, K.; et al. Giant Tunneling Magnetoresistance in Spin-Filter van der Waals Heterostructures. *Science* **2018**, *360*, 1214–1218. [CrossRef] [PubMed]
44. Jiang, S.; Li, L.; Wang, Z.; Shan, J.; Mak, K.F. Spin Tunnel Field-Effect Transistors Based on Two-Dimensional van der Waals Heterostructures. *Nat. Electron.* **2019**, *2*, 159–163. [CrossRef]
45. Zhan, P.; Wang, W.; Liu, C.; Hu, Y.; Li, Z.; Zhang, Z.; Zhang, P.; Wang, B.; Cao, X. Oxygen Vacancy-Induced Ferromagnetism in Undoped ZnO Thin Films. *J. Appl. Phys.* **2012**, *111*, 033501–1–033501–5. [CrossRef]
46. Rajan, C.P.; Abharana, N.; Jha, S.N.; Bhattacharyya, D.; John, T.T. Local Structural Studies Through EXAFS and Effect of Fe^{2+} or Fe^{3+} Existence in ZnO Nanoparticles. *J. Phys. Chem. C* **2021**, *125*, 24, 13523–13533. [CrossRef]
47. Cheng, W.; Ma, X. Structural, Optical and Magnetic Properties of Fe-Doped ZnO. *J. Phys. Conf. Ser.* **2009**, *152*, 012039. [CrossRef]
48. Beltrán, J.J.; Barreroa, C.A.; Punnoose, A. Understanding the Role of Iron in the Magnetism of Fe-Doped ZnO Nanoparticles. *Phys. Chem. Chem. Phys.* **2015**, *17*, 15284–15296. [CrossRef]

Disclaimer/Publisher's Note: The statements, opinions and data contained in all publications are solely those of the individual author(s) and contributor(s) and not of MDPI and/or the editor(s). MDPI and/or the editor(s) disclaim responsibility for any injury to people or property resulting from any ideas, methods, instructions or products referred to in the content.